



Relating the surface topography of as-built Inconel 718 surfaces to laser powder bed fusion process parameters using multivariate regression analysis

Sean Detwiler, Dillon Watring, Ashley Spear, Bart Raeymaekers*

Department of Mechanical Engineering, University of Utah, Salt Lake City, UT, 84112, USA

ARTICLE INFO

Keywords:

L-PBF
Additive manufacturing
Multivariate regression
Surface topography

ABSTRACT

The surface topography of 3D printed parts differs from that of wrought or machined parts of the same material. This work specifically focuses on Inconel 718 specimens manufactured with laser powder bed fusion (L-PBF). Predicting the surface topography of the as-built surfaces based on the L-PBF process parameters is important to manufacture parts with a specific surface topography without costly post-processing. We measure the surface topography of Inconel 718 as-built surfaces manufactured with different bulk and contour laser power, scan speed, layer thickness, and build orientation, and perform multivariate regression analysis with traditional R - and S -parameters, statistical and deterministic parameters, and even combinations of surface topography parameters, to determine which parameters most closely relate to the L-PBF process parameters. The deterministic surface topography parameters derived from a 9-point peak-identification scheme resulted in the best-fit regression equations with the highest adjusted- R^2 and, thus, showed the closest relationship to the L-PBF process parameters. In contrast to the R -, S -, and statistical parameters, the deterministic approach considers the actual peaks of the surface topography rather than relying on a discrete number of traces of the surface. This conclusion is different from existing knowledge on the surface topography of as-built L-PBF surfaces, which only considers traditional R - and S -parameters.

1. Introduction

Powder bed fusion is a class of additive manufacturing (AM) techniques that includes selective laser melting (SLM), which is also known as laser powder bed fusion (L-PBF) and electron beam melting (EBM) [1, 2]. L-PBF uses a laser to selectively melt and fuse metal powder particles in a layer-upon-layer fashion [3,4] and, thus, enables manufacturing specimens with complex three-dimensional (3D) geometry that cannot be manufactured with traditional subtractive methods [5,6], e.g. for use in biomedical [7] or aerospace [8] applications. The L-PBF process has been advanced in recent years by expanding the number of printable metals [9], increasing process speed and throughput, and tuning the process parameters for improved print quality [10].

However, L-PBF parts often require costly post-processing techniques to modify the surface topography of the as-built surfaces before they can be used in engineering applications. Three common methods exist [11]; heat treatment including hot isostatic pressing [12,13] and annealing [14] to reduce porosity [15] and surface roughness [6]; chemical

treatment [16,17] to remove unmelted metal powder particles from the as-built surfaces; and mechanical treatment such as shot peening to modify surface topography through mechanical impact [18,19].

Predicting the surface topography of the as-built surfaces based on the L-PBF process parameters is crucial to designing and manufacturing parts with user-specified surface topography that does not require post-processing. It is well-known that increasing contour laser power and laser energy density, which depends on laser power, laser scan speed, hatch spacing, and layer thickness, increases the size of the melt pool. Furthermore, increasing the laser scan speed increases the temperature gradient between the melt pool and previously melted tracks [20], and decreases the melt pool size because the energy of the laser beam distributes over a larger area [21].

Even though the properties of the melt pool, driven by the L-PBF process parameters, have a substantial effect on the surface topography of the as-built surfaces, their relationship is currently not well-understood. Recent publications have attempted to shed light on this relationship using trial-and-error methods, regression analysis, and

* Corresponding author.

E-mail address: bart.raeymaekers@utah.edu (B. Raeymaekers).

machine learning methods.

Several researchers have performed parameter studies in trial-and-error fashion. Triantaphyllou et al. [22] documented that surface topography parameters (Ra , Sa , Sq , and Ssk) of as-built surfaces of Ti–6Al–4V SLM and EBM parts allow distinguishing the up-facing from the down-facing surfaces, especially using the skewness Ssk . Specifically, they explained that unmelted metal powder particles adhere to the down-facing surfaces whereas pits exist on the up-facing surfaces. This results in a more symmetric surface height distribution of the former than the latter as-built surfaces, which is represented in the skewness parameter Ssk . Eidt et al. [23] studied the effect of bulk laser power and scan speed on the surface topography of vertical and down-facing surfaces of Inconel 718 L-PBF parts and observed that the surface topography parameters (Sa , Sq , Sv , and Sp) decrease with increasing bulk laser power and appear almost independent of scan speed. They explained that the melt pool size increases with increasing bulk laser power, which increases overlap between adjacent melt tracks, “smoothens” the surface topography, and decreases the number of peaks and valleys on the as-built surface. Strano et al. [24] compared the surface roughness (Ra) measurements of the up-facing surfaces of a 316L steel truncheon test specimen to the values they determined using a mathematical model that accounts only for the part geometry (build orientation and layer thickness). They concluded that a model solely based on material geometry does not accurately predict the surface roughness (Ra) for up-facing surfaces, in part because it neglects unmelted metal powder particles that adhere to the as-built surfaces.

Multivariate regression analysis has also been used to relate the surface topography of the as-built surfaces to the L-PBF process parameters. Calignano et al. [18] studied the effect of contour laser power, scan speed, and hatch spacing on the surface roughness (Ra) of the up- and down-facing surfaces of AlSi10Mg parts, and used linear regression to relate the surface roughness (Ra) to the process parameters ($R^2 = 0.7$). Furthermore, they observed that the surface roughness (Ra) increases with increasing contour laser power and hatch spacing because liquid metal ejection from the melt pool increases with increasing contour laser power, and the gaps between melted tracks increase with increasing hatch spacing, which increases the number of peaks and valleys on the as-built surface. Charles et al. [25] studied the effect of L-PBF process parameters and build orientation on the surface roughness (Sa) of down-facing as-built surfaces of Ti–6Al–4V L-PBF parts, and observed that the surface roughness (Sa) decreases with increasing contour laser power and increasing build orientation because the melt pool size increases with increasing contour laser power, thus increasing overlap between adjacent melt tracks. Furthermore, the size of the solidified layer below the melt pool increases with increasing build orientation, which increases heat conduction away from unmelted metal powder particles and, thus, results in fewer partially melted metal powder particles that adhere to the down-facing as-built surface. Fox et al. [26] evaluated the effect of build orientation, contour laser power, and scan speed on the surface topography of the as-built down-facing surfaces of stainless steel L-PBF parts, and observed that the peak count (Rpc) decreases and the mean element profile width (Rsm) and mean element profile height (Rc) increases with decreasing build orientation. They attributed this result to the number of unmelted metal powder particles that adhere to the as-built surfaces, which increases with decreasing build orientation, similar to the observations of Charles et al. [25]. However, they did not document a statistically significant relationship between the surface topography parameters and the contour laser power or scan speed.

The relationship between the surface topography and the L-PBF process parameters is not only relevant to the up- or down-facing as-built surfaces, but also the side surfaces. Thus, several researchers have used multivariate regression analysis considering the surface topography of all as-built surfaces. Safdar et al. [27] studied the effect of part thickness, beam current, offset focus, and scan speed, on the surface roughness (Ra) of EBM printed Ti–6Al–4V as-built surfaces and

documented that the surface roughness (Ra) increases with increasing part thickness and beam current and decreases with increasing offset focus and scan speed. They derived a best-fit equation that relates the surface roughness (Ra) of any side surface (i.e., parallel to the build direction and orthogonal to the top surface) to the EBM process parameters and obtained an adjusted- R^2 of 0.989. Galati et al. [28] studied the effect of build orientation on the surface roughness (Ra) of up-facing and down-facing as-built surfaces for EBM printed Ti–6Al–4V, and showed that the surface roughness (Ra) increases and decreases for up- and down-facing as-built surfaces, respectively, with increasing build orientation. Whip et al. [29] studied the effect of contour laser power and scan speed on the S - and R -parameters of as-built Inconel 718 L-PBF surfaces and determined that R -parameters are inaccurate metrics to describe the surface topography of AM parts because unmelted metal powder particles that are not representative of the actual surface topography of the as-built surface may corrupt them. They also observed that the melt pool size increases with increasing contour laser power and decreasing scan speed, thus decreasing the surface topography parameters (Sa , Sv , $Smr2$, and Svk) because increasing melt pool size increases overlap between adjacent melt tracks.

Furthermore, Khorasani et al. [30] used an artificial neural network (ANN) to relate the surface roughness (Sa) of as-built Ti–6Al–4V surfaces to the L-PBF process parameters, including contour laser power, scan speed, hatch spacing, and pattern angle, as well as post-processing heat treatment, and they determined a correlation coefficient greater than 95.3% between ANN model predictions and experimental data. In addition, they showed that the surface roughness (Sa) increases with increasing contour laser power and decreasing scan speed because gas entrapment in the melt pool causes keyholes. These results contrast those documented by Eidt et al. [23] and Charles et al. [25] who only analyzed down-facing as-built surfaces. Özel et al. [31] used genetic programming and an ANN to relate the surface topography parameters (Sa , Sq , Ssk , and Sku) of the up-facing as-built surfaces to energy density, scan speed, and contour laser power, and predicted those surface topography parameters with an average prediction error of 5.5%, 1.1%, 7.4%, and 18%, respectively.

The literature shows that research into the relationship between L-PBF process parameters and the corresponding surface topography of as-built surfaces has mostly focused on using the traditional R - and S -parameters. Moreover, most publications only consider the average surface roughness parameters (Ra and Sa for a trace and surface, respectively), in addition to less common surface topography parameters (Sq , Sv , Sp , Ssk , and Sku). Furthermore, the context of these studies is primarily geared towards relating the surface topography of as-built surfaces to the fatigue life of L-PBF parts. However, no publications evaluate the relationship between other metrics that quantify or describe the surface topography of the as-built surfaces and the L-PBF process parameters. Since it is well-known that e.g., the average surface roughness (Ra or Sa) does not unambiguously quantify the surface topography of engineering surfaces [32], other metrics, including statistical and deterministic parameters, might more closely relate the surface topography of the as-built surfaces and L-PBF process parameters. Furthermore, those parameters can be determined from the same surface topography measurement than that to calculate R - and S -parameters.

Thus, the objective of this paper is to determine the relationship between the surface topography parameters of as-built Inconel 718 surfaces and their corresponding L-PBF process parameters. We measure the surface topography of as-built Inconel 718 surfaces, manufactured with different bulk and contour laser power, scan speed, layer thickness, and build orientation, and we use multivariate regression analysis with traditional R - and S -parameters, statistical and deterministic parameters, and even combinations of surface topography parameters, to determine which parameters most closely relate to the L-PBF process parameters. In addition, we attempt to explain the physical mechanisms underlying the experimental observations.

2. Methods and materials

2.1. Specimen fabrication

We use Inconel 718 specimens manufactured with an L-PBF printer (3D Systems ProX DMP 320) and recycled 3D Systems IN718 powder that follows ASTM F1877 for particle size and aspect ratio distribution [33]. Fig. 1 schematically illustrates the build plate, indicating the location and build orientation (0° (red), 60° (blue), 90° (green)) of 75 standard $101.60 \text{ mm} \times 19.05 \text{ mm} \times 3.10 \text{ mm}$ (fatigue) specimens that follow ASTM E466-07 [34], which we previously used for fatigue experiments in Refs. [35,36]. Fig. 1 also introduces a numbering scheme for the five as-built surfaces (S1 – S5) of the specimens. The recoater, which creates a uniform layer of metal powder prior to selective melting and solidification, travels from S1 to S2 (positive x -direction) and the gas flows from S3 to S4 (positive y -direction). Inert gas flow during the L-PBF process prevents oxidation of the metal and evacuates process emissions from the melt pool to preserve an unobstructed path between the laser and the powder bed [37]. S5 is the top surface of the specimens, orthogonal to the build direction (positive z -direction).

Table 1 lists the different L-PBF process parameters of each of the 24 specimens we used in this work for surface topography measurements (selected out of 75 specimens, originally printed on the build plate for fatigue experiments [35,36]). These parameters include bulk laser power $115 \text{ W} \leq P \leq 465 \text{ W}$, laser scan speed $620 \text{ mm/s} \leq v \leq 1770 \text{ mm/s}$, layer thickness $t = 30 \text{ }\mu\text{m}$ or $t = 60 \text{ }\mu\text{m}$, build orientation $\alpha = 0^\circ$, 60° , or 90° , and the (volumetric) laser-energy density $E_p = P/vht$, which is a function of the laser power P , laser scan speed v , layer thickness t , and the hatch spacing h . We used a constant contour laser power of 115 W and 165 W for the specimens with $t = 30 \text{ }\mu\text{m}$ and $t = 60 \text{ }\mu\text{m}$, respectively, independent of the build orientation. The parameter sets were chosen to maintain $30 \text{ J/mm}^3 \leq E_p \leq 90 \text{ J/mm}^3$, which is the range that 3D Systems recommends, and to include parameter sets for each build orientation (0° , 60° , 90°) that span the range $30 \text{ J/mm}^3 \leq E_p \leq 90 \text{ J/mm}^3$. All other parameters remained constant, using standard 3D Systems specifications, i.e., a contour scan speed of 625 mm/s, hatch spacing of 100 μm , and laser spot size of 50 μm .

2.2. Surface topography measurement

Three techniques are commonly used to measure the surface topography of L-PBF specimens [38,39]; optical profilometry, confocal laser scanning microscopy (CLSM), and scanning electron microscopy (SEM). Based on specimen size, size of surface topography features,

resolution and accuracy [40], we used a CLSM (Olympus LEXT OLS5000) to measure the surface topography of the as-built surfaces of all 24 specimens, with 0.006 μm vertical resolution, 0.625 μm lateral resolution (20X optical zoom), and 1.8 mm \times 1.8 mm field-of-view, selected based on convergence studies.

Fig. 2 (a) shows a photograph of a typical L-PBF specimen, schematically indicating its relationship to the original fatigue specimen, and Fig. 2 (b) identifies the different as-built surfaces of the specimen (gray shaded). Note that surfaces A, B, C, and D correspond to four as-built surfaces out of S1–S5, depending on their location and orientation on the build plate (see Fig. 1). Surfaces E and F are not as-built surfaces; for specimens built with $\alpha = 0^\circ$ surfaces E and F correspond to S1 and S2 and for specimens built at $\alpha = 60^\circ$ and $\alpha = 90^\circ$ surface E corresponds to S5. We only consider as-built surfaces in this analysis. Fig. 2 (b) indicates the different surface topography measurement locations on each as-built surface; we perform twelve measurements per specimen (four as-built surfaces and three locations on each as-built surface). Fig. 2 (c) and (d) illustrate two typical surface topography measurements for specimen 2.

We correct the surface topography data $z = f(x,y)$ of each measurement for specimen tilt, and perform high-pass trace and areal digital filtering using a 9th-order high-pass Butterworth filter (which maximizes frequency response function roll-off), to separate the roughness (R -profile) from the surface topography (P -profile) and the areal surface roughness (SL -surface) from the primary surface, respectively, according to ISO 25178-2 [41]. Specifically, it removes the large wavelength components caused by the track-by-track L-PBF process from the surface topography, only leaving the roughness (R -profile and SL -surface). The cutoff frequency of the high-pass 9th-order Butterworth filter derives from a convergence analysis of Ra for a trace of the surface and Sa for the entire surface. We did not attempt to filter high spatial frequency measurement noise.

2.3. Surface topography parameters

We calculate the surface topography parameters from the high-pass filtered surface topography data. We determine the R - and S -parameters over the length of each measurement location because they are independent of the evaluation length, but the variability of the measurements decreases with increasing evaluation length. We consider the mean height (Ra/Sa), the average maximum height of the profile (Rz/Sz), the maximum positive deviation from the mean plane (Rp/Sp), the maximum negative deviation from the mean plane (Rv/Sv), the root mean square deviation (Rq/Sq), the skewness (Rsk/Ssk), and the kurtosis

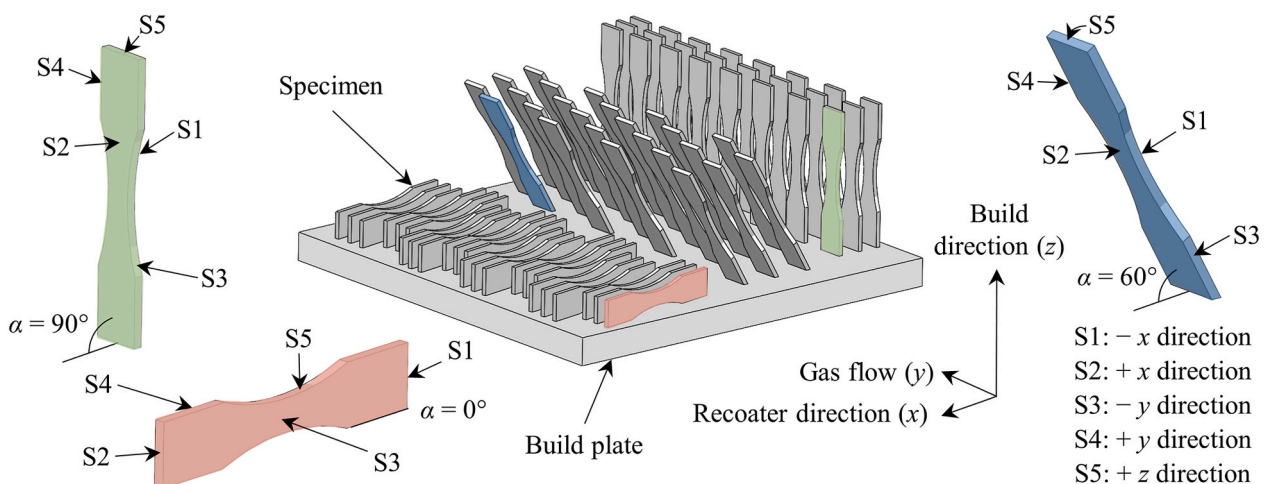


Fig. 1. Schematic of the build plate, indicating the location and build orientation of the specimens, and identifying the different as-built surfaces (S1–S5) of the specimens. A Cartesian coordinate system indicates the recoater movement (S1 to S2) in the x -direction, gas flow (S3 to S4) in the y -direction, and build direction (S5) in the z -direction.

Table 1
List of specimens and their corresponding L-PBF process parameter values.

| Specimen number | Contour laser power [W] | Bulk laser power [W] | Laser scan speed [mm/s] | Layer thickness [μm] | Build orientation [$^\circ$] | Energy density [J/mm^3] |
|-----------------|-------------------------|----------------------|-------------------------|-----------------------------------|--------------------------------|---|
| 1 | 115 | 220 | 1180 | 30 | 60 | 62.15 |
| 2 | 115 | 220 | 1180 | 30 | 60 | 62.15 |
| 3 | 115 | 330 | 1770 | 30 | 0 | 62.15 |
| 4 | 115 | 115 | 620 | 30 | 90 | 61.83 |
| 5 | 115 | 115 | 620 | 30 | 90 | 61.83 |
| 6 | 115 | 168 | 1475 | 30 | 0 | 37.97 |
| 7 | 115 | 168 | 1475 | 30 | 0 | 37.97 |
| 8 | 115 | 275 | 1200 | 30 | 0 | 76.39 |
| 9 | 115 | 115 | 915 | 30 | 60 | 41.89 |
| 10 | 115 | 330 | 1475 | 30 | 60 | 74.58 |
| 11 | 115 | 168 | 1180 | 30 | 90 | 47.46 |
| 12 | 115 | 200 | 800 | 30 | 90 | 83.33 |
| 13 | 115 | 275 | 1770 | 30 | 60 | 51.79 |
| 14 | 165 | 315 | 1050 | 60 | 60 | 50.00 |
| 15 | 165 | 165 | 850 | 60 | 0 | 32.35 |
| 16 | 165 | 390 | 1050 | 60 | 60 | 61.90 |
| 17 | 165 | 465 | 1400 | 60 | 90 | 55.36 |
| 18 | 165 | 240 | 1250 | 60 | 60 | 32.00 |
| 19 | 165 | 390 | 1450 | 60 | 90 | 44.83 |
| 20 | 115 | 220 | 1180 | 30 | 90 | 62.15 |
| 21 | 165 | 315 | 1050 | 60 | 0 | 50.00 |
| 22 | 165 | 315 | 1050 | 60 | 90 | 50.00 |
| 23 | 165 | 315 | 1050 | 60 | 90 | 50.00 |
| 24 | 165 | 200 | 1000 | 60 | 90 | 33.33 |

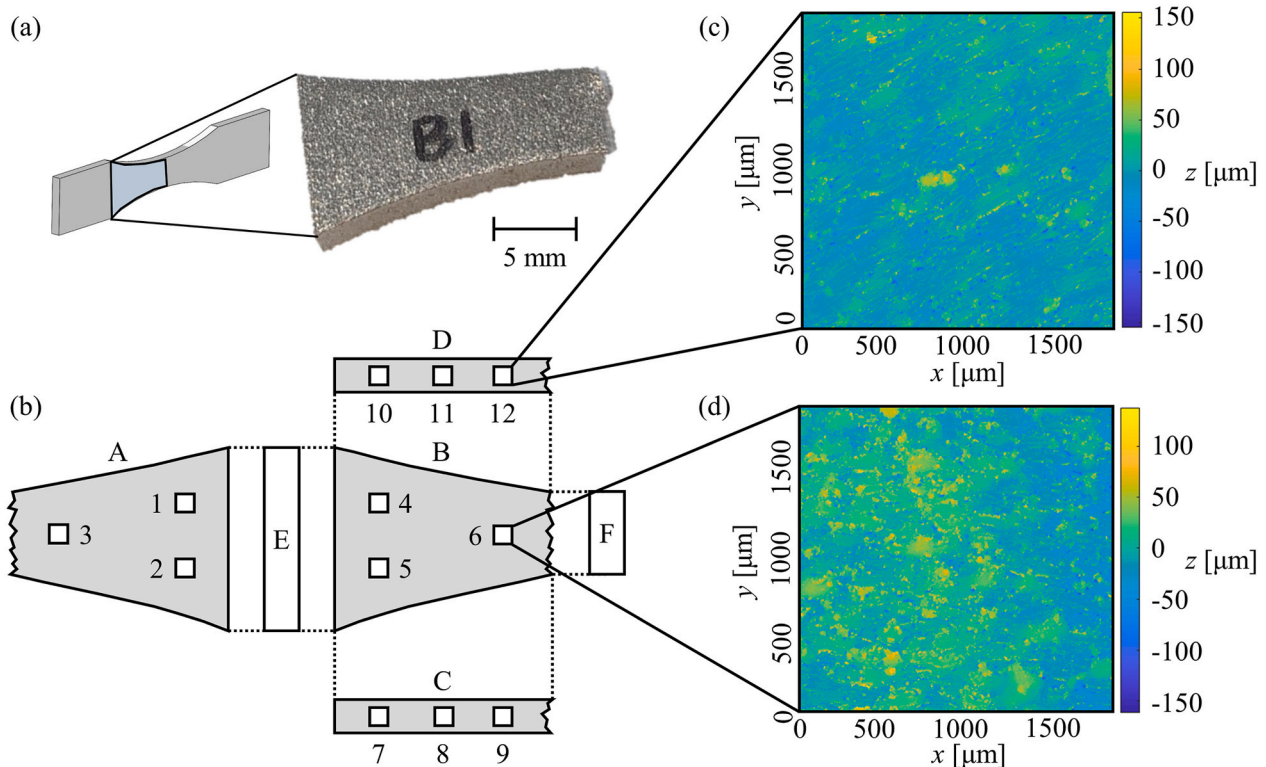


Fig. 2. (a) Photograph of a typical L-PBF specimen used in this work, and (b) schematic of the different as-built surfaces of the specimen (A–D), identifying the different surface topography measurement locations (1–12). Surfaces A, B, C, and D map to four surfaces of S1–S5, depending on their location and orientation on the build plate. Surfaces E and F are not as-built surfaces. (c) and (d) illustrate typical surface topography measurements (specimen 2).

(Rku/Sku) (see ISO 4287 [42] and ISO 25178-2 [41]). We quantify the R -parameters for each digital trace of $z = f(x,y)$ in the x - and y -directions and report the average R -parameters for all traces [42]. ISO 4287 specifies that the direction of a trace should cross the preferential direction of the surface topography, for instance resulting from a machining process. However, this direction is not defined unambiguously for the L-PBF process because the laser does not follow a uni-directional path and the recoater blade direction also comes into

play. Furthermore, R -parameters can vary substantially between single traces. Therefore, based on earlier work [43], averaging the R -parameters over multiple traces yields repeatable results.

We also use a statistical method derived by McCool [44], which quantifies the surface topography parameters based on the spectral moments m_0 , m_2 , and m_4 of a single, arbitrary trace $z(x)$ of a surface with isotropic surface topography. The spectral moments are

$$m_0 = \text{AVG}[(z^2)], \tag{1}$$

$$m_2 = \text{AVG}\left[\left(\frac{\partial z}{\partial x}\right)^2\right], \tag{2}$$

$$m_4 = \text{AVG}\left[\left(\frac{\partial^2 z}{\partial x^2}\right)^2\right], \tag{3}$$

where the AVG operator calculates the arithmetic mean. The surface topography parameters follow from the spectral moments, including the summit density η , the average summit radius R_s , and the standard deviation of summit heights σ_s , i.e.,

$$\eta = \left(\frac{m_4}{m_2}\right) / 6\pi\sqrt{3} \tag{4}$$

$$R_s = 0.375\sqrt{\frac{\pi}{m_4}} \tag{5}$$

$$\sigma_s = \sqrt{1 - \frac{0.8968}{\alpha_c}}\sqrt{m_0}, \tag{6}$$

with $\alpha_c = (m_0m_4)/m_2^2$ the bandwidth parameter. η , R_s , and σ_s may vary considerably for different, arbitrary selected traces [45]. Furthermore, the surface topography parameters calculated from the spectral moments also depend on the finite difference discretization scheme used to calculate the derivatives in Eqs. (2) and (3) [43,44]. While several schemes can be used, and the results obtained with different schemes can be related to each other [43], we used central finite difference discretization throughout this work for consistency. We calculate the spectral moments and corresponding η , R_s , and σ_s for each digital trace of $z = f(x,y)$ in the x - and y -directions and report the average η , R_s , and σ_s for all traces.

We also calculate deterministic surface topography parameters from the surface topography measurements that, in contrast with R -, S -parameters, and statistical methods, consider the entire surface topography rather than a single or a discrete number of traces. We determine the peaks of the surface topography as the local maxima using a 5- or 9-point peak (5 PP or 9 PP) identification scheme [43,45].

The standard deviation of summit heights σ_s results directly from the peaks, and the summit density $\eta = N/A_n$, with N the number of peaks and A_n the nominal surface area of the surface topography measurement (1.8 mm \times 1.8 mm). The curvature of each peak i in two orthogonal directions is $\kappa_{x,i} = d^2z/dx^2$ and $\kappa_{y,i} = d^2z/dy^2$, and the radius of curvature ρ_i of that peak is the inverse of the average of its κ_x and κ_y , i.e., $\rho_i = -[(\kappa_{x,i} + \kappa_{y,i})/2]^{-1}$. The mean summit radius R_s is the arithmetic mean of all individual peak radii. Finally, $\beta = \eta R_s \sigma_s$ is a dimensionless roughness parameter.

Table 2 summarizes the surface topography parameters we calculate for each surface topography measurement of each specimen in this work, including R -, S -, statistical, and deterministic parameters.

Table 2
Summary of all surface topography parameters we consider in this work.

| Parameter type | Parameters |
|--------------------------|--|
| R -parameters | Ra , Rq , Rp , Rv , Rsk , and Rku |
| S -parameters | Sa , Sq , Sp , Sv , Ssk , and Sku |
| Statistical parameters | Summit density η Mean summit radius R_s Standard deviation of summit heights σ_s |
| Deterministic parameters | Summit density (5 PP and 9 PP) Summit radius (5 PP and 9 PP) Standard deviation of summit heights (5 PP and 9 PP) Number of peaks (5 PP and 9 PP) N |

2.4. Multivariate regression analysis

Multivariate regression analysis relates the surface topography parameters (dependent variable) to the L-PBF process parameters, including bulk laser power P , laser scan speed v , volumetric energy density E_p , build orientation α , and layer thickness t (independent variables). The surface topography parameters that result from each measurement location are independent data points in the regression analysis, i.e., three measurement locations on each of the four as-built surfaces (see Fig. 2), for each of the 24 specimens, or 288 data points in total.

We first consider the surface topography of all as-built surfaces as one dataset, i.e., we do not distinguish between the different as-built surfaces S1–S5. Hence, we derive a best-fit regression equation that relates the surface topography parameters to the corresponding L-PBF process parameters, independent of any specific as-built surface. This represents a simplified approach because it is well-known that distinct differences exist between the surface topography of the as-built surfaces, depending on their orientation and location on the build plate. Nevertheless, it is a common approach in conventional manufacturing because existing standards do not specify a measurement location [41,42]. We also consider the surface topography of each as-built surface (S1–S5) as an individual dataset to determine the parameters that drive the surface topography of each distinct as-built surface. Thus, we derive a best-fit regression equation that relates the surface topography parameters to the corresponding L-PBF process parameters for each specific as-built surface.

Throughout this work, we only include significant terms (p -value $<$ 0.05) in the best-fit regression equations, and we only consider regression equations where all assumptions of the multivariate regression analysis are satisfied, i.e., the residuals are independent, homoscedastic, follow a normal distribution, and show no significant multicollinearity between independent variables [46]. We evaluate regression equations that include each process parameter individually, as well as linear, polynomial, exponential, and logarithmic combinations of (any) different process parameters to determine the best-fit regression equation that relates the surface topography parameters to the L-PBF process parameters. It is undesirable to split our small dataset in separate train and validation data to evaluate the prediction accuracy of the best-fit regression equations [47]. Instead, we quantify the goodness-of-fit using adjusted- R^2 [48], root mean square error (RMSE), and mean absolute error (MAE) [49] metrics.

2.5. Analysis of variance

We perform one-way ANOVA and Tukey’s honestly significant difference (HSD) tests to evaluate the average values of the surface topography parameters as a function of their location and orientation on the build plate, and as a function of the layer thickness. The dataset satisfies all assumptions for ANOVA and Tukey’s HSD tests, i.e., the residuals are independent, homoscedastic, and follow a normal distribution. A p -value of less than 0.05 corresponds to a statistically significant difference between the population means. However, we also report the actual p -values.

3. Results and discussion

3.1. Best-fit multivariate regression equations that relate surface topography parameters to L-PBF process parameters

Table 3 shows the surface topography parameters of Table 2, the best-fit regression equation for each parameter, and the corresponding adjusted- R^2 , MAE, and RMSE. Since adjusted- R^2 is dimensionless and scale-independent it provides a better comparison between surface topography parameters with different units than MAE and RMSE [50]. We determine that the deterministic surface topography parameters (η ,

Table 3

Surface topography parameters, best-fit regression equations, and corresponding adjusted-R², MAE, and RMSE. All regression coefficients are significant (i.e., p-value < 0.05). Table A1 in the supplemental information shows all p-values.

| Surface topography parameter | Best-fit regression equation | MAE | RMSE | ADJ-R ² |
|---------------------------------|---|-------|-------|--------------------|
| R-parameters | | | | |
| Ra | $Ra = 6.61 - 4.05 \cdot 10^{-3}P + 5.77 \cdot 10^{-4}v - 1.21 \cdot 10^{-2}\alpha$ | 0.813 | 1.094 | 0.287 |
| Rq | $Rq = 11.1 + 6.25 \cdot 10^{-4}v - 3.84 \cdot 10^{-2}t$ | 1.397 | 1.976 | 0.142 |
| Rp | $Rp = 80.8 - 0.10t - 0.13\alpha$ | 8.520 | 12.70 | 0.196 |
| Rv | $Rv = 81.7 - 0.13t - 9.68 \cdot 10^{-2}\alpha$ | 8.505 | 12.57 | 0.186 |
| Rsk | – | – | – | – |
| Rku | $Rku = 12.8 + 7.59 \cdot 10^{-2}P + 6.89 \cdot 10^{-3}t + 1.42 \cdot 10^{-2}\alpha$ | 2.360 | 3.401 | 0.315 |
| S-parameters | | | | |
| Sa | $Sa = 4.83 - 2.12 \cdot 10^{-3}P + 7.04 \cdot 10^{-4}v - 1.21 \cdot 10^{-2}t$ | 0.700 | 0.898 | 0.331 |
| Sq | $Sq = 7.74 - 7.16 \cdot 10^{-3}P + 1.36 \cdot 10^{-3}v - 1.83 \cdot 10^{-2}\alpha$ | 1.244 | 1.587 | 0.308 |
| Sp | – | – | – | – |
| Sv | – | – | – | – |
| Ssk | – | – | – | – |
| Sku | $Sku = 25.6 - 1.84 \cdot 10^{-2}v + 7.10 \cdot 10^{-2}\alpha + 3.06 \cdot 10^{-4}v\alpha$ | 0.104 | 0.135 | 0.257 |
| Statistical parameters | | | | |
| η | $\eta = 0.31 + 4.43 \cdot 10^{-5}P - 8.09 \cdot 10^{-5}\alpha$ | 0.014 | 0.020 | 0.120 |
| R _s | $R_s = 2.03 \cdot 10^{-2} + 1.14 \cdot 10^{-5}P - 1.93 \cdot 10^{-6}v + 4.50 \cdot 10^{-5}\alpha$ | 0.003 | 0.004 | 0.237 |
| σ _s | $\sigma_s = 10.2 - 5.48 \cdot 10^{-3}P + 9.94 \cdot 10^{-4}v - 1.74 \cdot 10^{-2}\alpha$ | 1.123 | 1.495 | 0.299 |
| Deterministic parameters | | | | |
| η (5 PP) | $\eta = 0.14 + 7.27 \cdot 10^{-4}t + 1.10 \cdot 10^{-4}\alpha$ | 0.018 | 0.022 | 0.255 |
| R _s (5 PP) | $R_s = 7.75 \cdot 10^{-2} + 6.23 \cdot 10^{-4}t + 1.30 \cdot 10^{-4}\alpha$ | 0.011 | 0.013 | 0.411 |
| σ _s (5 PP) | $\sigma_s = 11.2 - 6.77 \cdot 10^{-2}t - 2.61 \cdot 10^{-2}\alpha$ | 1.169 | 1.510 | 0.507 |
| N (5 PP) | $N = 4.47 \cdot 10^5 + 2.51 \cdot 10^3t + 352\alpha$ | 56380 | 70460 | 0.286 |
| η (9 PP) | $\eta = 0.10 + 7.89 \cdot 10^{-4}t + 8.17 \cdot 10^{-5}\alpha$ | 0.014 | 0.017 | 0.409 |
| R _s (9 PP) | $R_s = 8.49 \cdot 10^{-2} + 4.91 \cdot 10^{-5}P + 1.62 \cdot 10^{-4}\alpha$ | 0.010 | 0.013 | 0.257 |
| σ _s (9 PP) | $\sigma_s = 10.1 - 7.50 \cdot 10^{-3}P - 3.57 \cdot 10^{-2}\alpha$ | 1.555 | 1.968 | 0.382 |
| N (9 PP) | $N = 3.25 \cdot 10^5 + 2.51 \cdot 10^3t + 264\alpha$ | 42890 | 52960 | 0.412 |

R_s and σ_s) derived from the 9 PP scheme provide the best relationship to the L-PBF process parameters based on the adjusted-R² metric when considering one dataset of all as-built surfaces (S1–S5). Some parameters did not yield a regression equation that satisfies all assumptions of multivariate regression analysis, specified in Section 2.5. All regression coefficients are significant (i.e., p-value < 0.05). Additionally, Table A1 in the supplemental information shows all p-values. Note also that the input to the layer thickness process parameter is t = 30 μm or t = 60 μm, because this dataset only includes two different values of the layer thickness, and the build orientation is limited to vertical (α = 0° and α = 90°) and α = 60° specimens.

From Table 3 we observe that for all surface topography parameters, the best-fit regression equations result in adjusted-R² values below 0.5. Also, regression equations with adjusted-R² > 0.1 only exist for half of the S-parameters, suggesting that no close relationship exists between that type of surface topography parameters and the L-PBF process parameters. The R- and statistical parameters, which are based on digital traces of the surface, show an average adjusted-R² of 0.225 and 0.219, respectively. In comparison, the S- and deterministic (9 PP and 5 PP) parameters, which are based on the entire surface, show an average adjusted-R² of 0.298, 0.365 (9 PP), and 0.365 (5 PP), respectively. Unlike the R-, S-, and statistical parameters, the deterministic approach considers the actual peaks of the surface topography and, thus, results in best-fit regression equations with the highest adjusted-R². The build orientation α appears in each best-fit regression equation, except root mean square deviation Rq and average roughness Sa, indicating that the build orientation has an effect on almost all surface topography parameters, as expected from the literature (see e.g., Refs. [24–26]). Finally, Table 3 shows that all best-fit regression equations are linear, which is similar to what other papers have documented [18,25–27,29]. For instance, Liu et al. [20] determined a linear relationship between the L-PBF melt pool energy and laser scan speed and laser power. Similarly, Keshavarzkermani et al. [21] and Yadroitsev et al. [51] experimentally determined linear relationships between the melt pool size and laser power (150–300 W) and scan speed (30–240 mm/s), respectively.

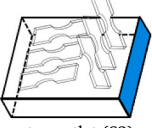
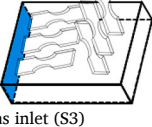
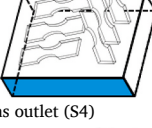
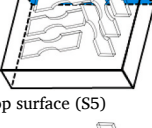
It is well-known that the directions of the recoater movement and gas flow, build orientation, and specimen proximity on the build plate,

among other factors, influence the surface topography of the different as-built surfaces of the specimens (see e.g., Refs. [26,52]). Hence, instead of aggregating the surface topography information of the different as-built surfaces into one dataset, we consider the surface topography information of the different as-built surfaces separately (see Fig. 1, S1–S5). Table 4 shows the five different as-built surfaces (S1–S5) (blue shaded), schematically indicating their location with reference to the build plate (see also Fig. 1). For each as-built surface, Table 4 lists the surface topography parameter for which we determined the best-fit regression equation with the highest adjusted-R². Table 4 also shows the best-fit regression equation for Ra and Rq with their respective adjusted-R² because these two metrics are commonly used in other publications. All adjusted-R² values of the best-fit equations are greater than 0.1. All regression coefficients are significant (i.e., p-value < 0.05). Additionally, Table A2 in the supplemental information shows all p-values.

From Table 4, we observe that the best-fit regression equations for different as-built surfaces involve different surface topography parameters, i.e., not a single parameter can be used to compare the surface topography of different as-built surfaces. The adjusted-R² values of the best-fit regression equations are substantially higher than those of Table 3, by considering the surface topography measurements of each different as-built surface separately, rather than aggregating them in one dataset. However, for three out of five different as-built surfaces (S2, S4, and S5) the deterministic (9 PP) surface topography parameters still relate most closely to the L-PBF process parameters, likely because they consider the actual peaks and, thus, include the most detailed information about the surface topography. Notably, when determining the surface topography parameter that results in the best-fit regression equation with the highest adjusted-R² for each as-built surface individually, the adjusted-R² is on average 50.5% higher compared to using the best-fit regression equation based on Ra. Furthermore, all best-fit regression equations include a term for the build orientation α, except for the top surface S5, indicating that the surface topography of all as-built surfaces except S5 depends on the build orientation. The latter result is similar to those presented in Ref. [38], which also show that the build orientation does not affect the surface topography of the top

Table 4

Different as-built surfaces (S1–S5) in blue, the best-fit regression equation of the surface topography parameter with the highest adjusted-R², and the best-fit regression equation of Ra and Rq, with their respective adjusted-R². All regression coefficients are significant (i.e., p-value < 0.05). Table A2 in the supplemental information shows all p-values.

| As-built surface ID | Surface topography parameter | Best-fit regression equation | MAE | RMSE | ADJ-R ² |
|---|------------------------------|--|-------|-------|--------------------|
| Recoater inlet (S1)  | Sa | $Sa = 3.58 + 3.24 \cdot 10^{-3}P - 1.48 \cdot 10^{-3}v + 2.41 \cdot 10^{-2}\alpha - 4.61 \cdot 10^{-2}t$ | 0.433 | 0.505 | 0.684 |
| | Ra | $Ra = 6.19 - 3.85 \cdot 10^{-3}P - 2.19 \cdot 10^{-3}v + 1.50 \cdot 10^{-2}\alpha - 4.26 \cdot 10^{-2}t$ | 0.429 | 0.525 | 0.660 |
| | Rq | $Rq = 11.4 - 6.17 \cdot 10^{-3}P - 3.13 \cdot 10^{-3}v - 5.80 \cdot 10^{-2}t$ | 0.724 | 0.862 | 0.505 |
| Recoater outlet (S2)  | R _s (9 PP) | $R_s = 2.20 \cdot 10^{-2} + 6.68 \cdot 10^{-5}P + 9.82 \cdot 10^{-4}\alpha$ | 0.008 | 0.011 | 0.760 |
| | Ra | $Ra = 6.83 - 5.71 \cdot 10^{-3}P + 1.99 \cdot 10^{-3}v - 2.53 \cdot 10^{-2}\alpha$ | 0.457 | 0.581 | 0.605 |
| | Rq | $Rq = 13.8 - 5.96 \cdot 10^{-3}P - 6.16 \cdot 10^{-2}\alpha$ | 0.731 | 0.950 | 0.667 |
| Gas inlet (S3)  | Rku | $Rku = 13.5 + 1.30 \cdot 10^{-2}P + 5.54 \cdot 10^{-2}\alpha$ | 1.739 | 2.072 | 0.577 |
| | Ra | $Ra = 6.67 - 8.90 \cdot 10^{-3}\alpha + 8.38 \cdot 10^{-4}E_p$ | 0.917 | 1.184 | 0.247 |
| | Rq | – | – | – | – |
| Gas outlet (S4)  | σ _s (9 PP) | $\sigma_s = 9.22 - 7.02 \cdot 10^{-3}P + 1.60 \cdot 10^{-3}v - 2.77 \cdot 10^{-2}\alpha$ | 1.048 | 1.316 | 0.568 |
| | Ra | $Ra = 5.77 - 4.83 \cdot 10^{-3}P + 1.22 \cdot 10^{-3}v$ | 0.675 | 0.933 | 0.216 |
| | Rq | – | – | – | – |
| Top surface (S5)  | η (9 PP) | $\eta = 9.27 \cdot 10^{-2} - 1.34 \cdot 10^{-4}P + 1.73 \cdot 10^{-3}t$ | 0.012 | 0.014 | 0.750 |
| | Ra | $Ra = 7.78 - 1.25 \cdot 10^{-2}P + 2.49 \cdot 10^{-3}v$ | 0.912 | 1.072 | 0.492 |
| | Rq | $Rq = 13.6 - 2.79 \cdot 10^{-2}P - 5.04 \cdot 10^{-3}v$ | 1.615 | 1.912 | 0.522 |

surface of the specimens. The parameter E_p only appears in one equation for Ra of S3 (gas inlet), likely because E_p is constrained within a tight range due to L-PBF process requirements and, thus has a smaller influence than the other process parameters (P and v), which we vary over a larger range than that of E_p .

We also observe that the surface topography relates most closely to the L-PBF process parameters for the S2 (recoater outlet) and S5 (top) as-built surfaces because the best-fit regression equations of those as-built surfaces show the highest adjusted-R². This is because the surface topography of S2 and S5 remains mostly undisturbed from external effects (mechanical contact with the recoater or gas flow) for which we do not account in the multivariate best-fit regression equations. In contrast, the as-built surfaces at the gas inlet (S3) and outlet (S4) show best-fit regression equations with the lowest adjusted-R² and, thus, the surface topography of S3 and S4 relates least closely to the L-PBF process parameters. The gas flow disturbs the IN718 powder particles, which alters

the surface topography, similar to the results documented by Fox et al. [26]. The best-fit regression equation for the as-built surface at the gas inlet (S3) involves the kurtosis Rku , i.e., the “spikiness” of the surface topography, because the surface topography of S3 is affected by unmelted metal powder particles that adhere to the surface, driven by gas flow. Similarly, the recoater creates a mechanical disturbance of the unmelted metal powder particles, which also affects the resulting surface topography [52].

Table 5 shows the three highest adjusted-R² values (in descending order) that result from best-fit regression equations for each as-built surface (S1–S5), and their corresponding surface topography parameters. It includes deterministic surface topography parameters for each as-built surface, and the standard deviation of asperity heights σ_s appears for all surfaces except S1. We observe that the difference between the three highest adjusted-R² values is minimal for each as-built surface, thus illustrating that deterministic surface topography parameters relate more closely to the surface topography of the different as-built surfaces than traditionally used R - and S -parameters.

Table 5

Three highest adjusted-R² values that result from best-fit regression equations for each as-built surface (S1–S5) and the corresponding surface topography parameters.

| ADJ-R ² | Recoater inlet (S1) | Recoater outlet (S2) | Gas inlet (S3) | Gas outlet (S4) | Top surface (S5) |
|--------------------|----------------------------------|---|----------------------------------|----------------------------------|----------------------------------|
| 1 | Sa (0.684) | R _s (9 PP) (0.760) | Rku (0.577) | σ _s (9 PP) (0.568) | η (9 PP) (0.750) |
| 2 | Rku (0.672) | σ _s (9 PP) (0.735) | σ _s (9 PP) (0.514) | N (9 PP) (0.536) | N (9 PP) (0.741) |
| 3 | R _s (5 PP) (0.653) | σ _s (statistical) (0.687) | Sa (0.489) | η (9 PP) (0.532) | σ _s (9 PP) (0.738) |

3.2. Effect of the location and orientation of the specimen on the build plate on the predictability of the surface topography parameters

Table 6 shows the average and standard deviation of the 9 PP deterministic surface topography parameters (η , R_s , and σ_s) for each as-built surface of the specimens (S1–S5) and the p-values resulting from a Tukey’s honestly significant difference (HSD) test, which compares the average of each parameter for each as-built surface. We indicate significant values with “**” (i.e., p-value < 0.05).

From Table 6, we observe that no statistical difference exists between any combination of the deterministic (9 PP) surface topography

Table 6

Average and standard deviation of 9 PP deterministic surface topography parameters (η , R_s , and σ_s) of the five as-built surfaces (S1–S5) and corresponding p -values resulting from a comparison of the average of each deterministic parameter for each of the five as-built surfaces, using a Tukey’s HSD test. Significant p -values (i.e., p -value < 0.05) show with an “*”.

| average/standard deviation | | S1 | S2 | S3 | S4 | S5 |
|----------------------------|----|--------------------------|--------------------------|-------------------------|--------------------------|--------------|
| η (9 PP) | | 0.141/0.017 | 0.140/0.021 | 0.142/0.022 | 0.143/0.018 | 0.160/0.027 |
| R_s (9 PP) | | 0.098/0.012 | 0.096/0.018 | 0.094/0.015 | 0.096/0.012 | 0.087/0.010 |
| σ_s (9 PP) | | 7.299/1.869 | 7.683/2.301 | 7.976/2.416 | 7.586/1.847 | 10.908/0.305 |
| Tukey HSD p -values | | S1 | S2 | S3 | S4 | S5 |
| η (9 PP) | S2 | 9.99•10 ⁻¹ | – | – | – | – |
| | S3 | 9.98•10 ⁻¹ | 9.82•10 ⁻¹ | – | – | – |
| | S4 | 9.81•10 ⁻¹ | 9.23•10 ⁻¹ | 9.98•10 ⁻¹ | – | – |
| | S5 | 5.82•10 ⁻³ * | 3.08•10 ⁻³ * | 7.48•10 ⁻³ * | 1.37•10 ⁻² * | – |
| | S5 | 9.48•10 ⁻¹ | – | – | – | – |
| R_s (9 PP) | S2 | 5.14•10 ⁻¹ | – | – | – | – |
| | S3 | 5.14•10 ⁻¹ | 9.34•10 ⁻¹ | – | – | – |
| | S4 | 9.34•10 ⁻¹ | 1.00 | 9.14•10 ⁻¹ | – | – |
| | S5 | 3.60•10 ⁻² * | 1.34•10 ⁻¹ | 3.28•10 ⁻¹ | 1.12•10 ⁻¹ | – |
| σ_s (9 PP) | S2 | 8.68•10 ⁻¹ | – | – | – | – |
| | S3 | 3.60•10 ⁻¹ | 9.33•10 ⁻¹ | – | – | – |
| | S4 | 9.37•10 ⁻¹ | 9.99•10 ⁻¹ | 7.87•10 ⁻¹ | – | – |
| | S5 | 2.00•10 ⁻¹⁶ * | 2.00•10 ⁻¹⁶ * | 1.40•10 ⁻⁶ * | 2.00•10 ⁻¹⁶ * | – |
| | S5 | 2.00•10 ⁻¹⁶ * | – | – | – | – |

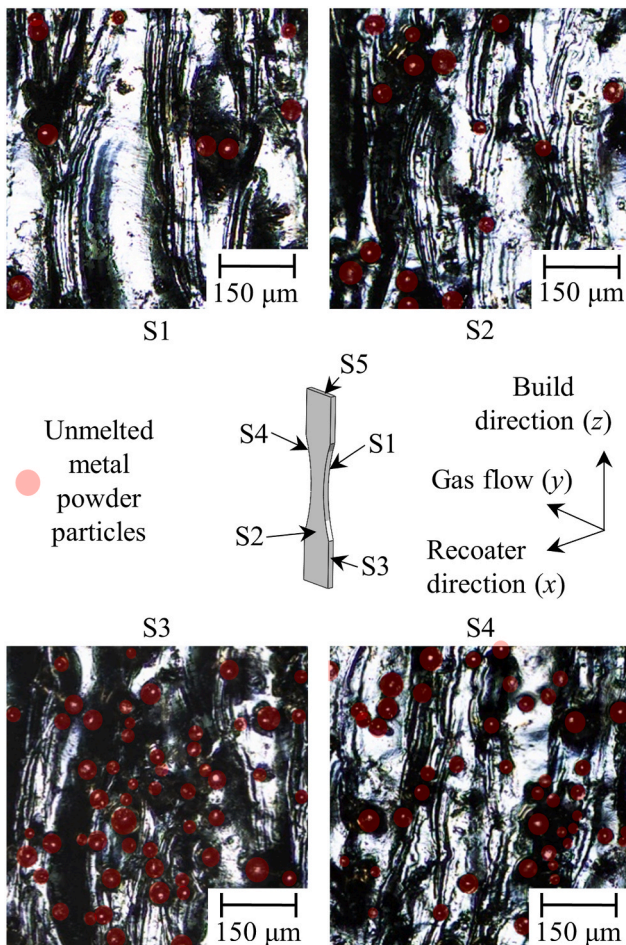


Fig. 3. Optical microscopy images of S1, S2, S3, and S4 for a specimen with $\alpha = 90^\circ$ (specimen 24), identifying unmelted metal powder particles on each of the as-built surfaces, and showing a lower density of unmelted metal powder particles (highlighted in red) in the recoater direction (S1 and S2) than in the gas flow direction (S3 and S4). (For interpretation of the references to colour in this figure legend, the reader is referred to the Web version of this article.)

parameters for the as-built surfaces in the recoater (S1, S2) and gas flow (S3, S4) directions, despite the different physical phenomena driving the surface topography of those respective as-built surfaces. For instance,

the build orientation drives the surface topography parameters of S1 and S2, whereas unmelted metal powder particles from the gas flow adhere to S3 and S4 and affect the resulting surface topography parameters, even though the unmelted metal powder particles are not actually part of the as-built surface [53]. Thus, the best-fit regression equations for S1 and S2 result in a higher adjusted- R^2 than for S3 and S4 (see Table 4) because the build orientation is an input parameter to the multivariate regression analysis and the number of particles adhering to the different as-built surfaces, driven by the gas flow, is not. Fig. 3 shows optical microscopy images of S1, S2, S3, and S4 of specimen 24 ($\alpha = 90^\circ$, $t = 60 \mu\text{m}$, $E_p = 33.3 \text{ J/mm}^3$) and illustrates that the density of unmelted metal powder particles (approximately $40 \mu\text{m}$ diameter and highlighted in red) that adhere to the different as-built surfaces depends on their orientation with respect to the gas flow direction.

From Fig. 3 we observe fewer unmelted metal powder particles on the as-built surfaces in the recoater direction (S1 and S2) than in the gas flow direction (S3 and S4), as expected. The unmelted metal powder particle density is approximately 25.0 unmelted metal powder particles/ mm^2 (S1), 41.7 unmelted metal powder particles/ mm^2 (S2), 152.8 unmelted metal powder particles/ mm^2 (S3), and 125.0 unmelted metal powder particles/ mm^2 (S4), which is typical for all specimens we have examined. These results are also in agreement with those documented by Li et al. [53] and Chen et al. [52], who determined that gas flow over the metal powder bed deposits unmelted metal powder particles on the as-built surfaces in the gas flow direction, which increases the surface topography parameters of those as-built surfaces.

3.3. Surface topography parameters as a function of layer thickness

Table 7 shows the average and standard deviation of the 9 PP deterministic surface topography parameters (η , R_s , and σ_s) for each as-built surface of the specimens (S1–S5), and for different layer thickness $t = 30 \mu\text{m}$ and $t = 60 \mu\text{m}$. The one-way ANOVA p -values show the effect of layer thickness on the deterministic surface topography parameters, and we indicate significant p -values with “*”.

From Table 7 we observe that the average values of the summit density η and mean summit radius R_s increase and the standard deviation of summit heights σ_s decreases with increasing layer thickness (from $t = 30 \mu\text{m}$ to $t = 60 \mu\text{m}$), i.e., the surface roughness decreases with increasing layer thickness. All deterministic parameters except R_s of S5 show a p -value of less than 0.05, demonstrating that the surface roughness decreases with increasing layer thickness. However, the number of summits also increases with increasing layer thickness because the number of globules increases. This is because increasing the layer thickness requires increasing the laser power or decreasing the

Table 7

Average and standard deviation of 9 PP deterministic surface topography parameters (η , R_s , and σ_s) and one-way ANOVA p -values show a comparison of average deterministic parameters, for $t = 30 \mu\text{m}$ and $t = 60 \mu\text{m}$ for the five as-built surfaces. Significant p -values (i.e., p -value < 0.05) show with an “*”.

| | | S1 | | S2 | | S3 | | S4 | | S5 | |
|-------------------|----------------------------|-------------------------|----------------------|-------------------------|----------------------|--------------------------|----------------------|-------------------------|----------------------|-------------------------|----------------------|
| | | $t = 30 \mu\text{m}$ | $t = 60 \mu\text{m}$ | $t = 30 \mu\text{m}$ | $t = 60 \mu\text{m}$ | $t = 30 \mu\text{m}$ | $t = 60 \mu\text{m}$ | $t = 30 \mu\text{m}$ | $t = 60 \mu\text{m}$ | $t = 30 \mu\text{m}$ | $t = 60 \mu\text{m}$ |
| η (9 PP) | Average/Standard deviation | 0.133/ 0.017 | 0.150/ 0.011 | 0.128/ 0.015 | 0.155/ 0.019 | 0.130/ 0.014 | 0.159/ 0.018 | 0.133/ 0.014 | 0.157/ 0.015 | 0.145/ 0.016 | 0.191/ 0.016 |
| | ANOVA p -value | 9.30•10 ⁻⁵ * | | 3.00•10 ⁻⁷ * | | 6.87•10 ⁻¹¹ * | | 1.47•10 ⁻⁹ * | | 2.98•10 ⁻⁵ * | |
| | | 0.092/ 0.011 | 0.106/ 0.007 | 0.085/ 0.016 | 0.108/ 0.013 | 0.086/ 0.008 | 0.105/ 0.013 | 0.090/ 0.011 | 0.104/ 0.008 | 0.086/ 0.010 | 0.092/ 0.009 |
| R_s (9 PP) | Average/Standard deviation | 1.59•10 ⁻⁶ * | 6.077/ 0.710 | 5.82•10 ⁻⁷ * | 9.075/ 1.924 | 5.943/ 1.354 | 9.166/ 0.858 | 6.310/ 2.467 | 8.473/ 1.811 | 6.346/ 0.980 | 12.39/ 2.969 |
| | ANOVA p -value | 2.48•10 ⁻⁶ * | | 1.26•10 ⁻⁸ * | | 1.52•10 ⁻⁹ * | | 1.48•10 ⁻⁷ * | | 3.27•10 ⁻³ * | |
| | | | | | | | | | | | |
| σ_s (9 PP) | Average/Standard deviation | 8.276/ 1.932 | 6.077/ 0.710 | 9.075/ 1.924 | 5.943/ 1.354 | 9.166/ 0.858 | 6.310/ 2.467 | 8.473/ 1.811 | 6.346/ 0.980 | 12.39/ 2.969 | 7.955/ 1.436 |
| | ANOVA p -value | 2.48•10 ⁻⁶ * | | 1.26•10 ⁻⁸ * | | 1.52•10 ⁻⁹ * | | 1.48•10 ⁻⁷ * | | 3.27•10 ⁻³ * | |
| | | | | | | | | | | | |

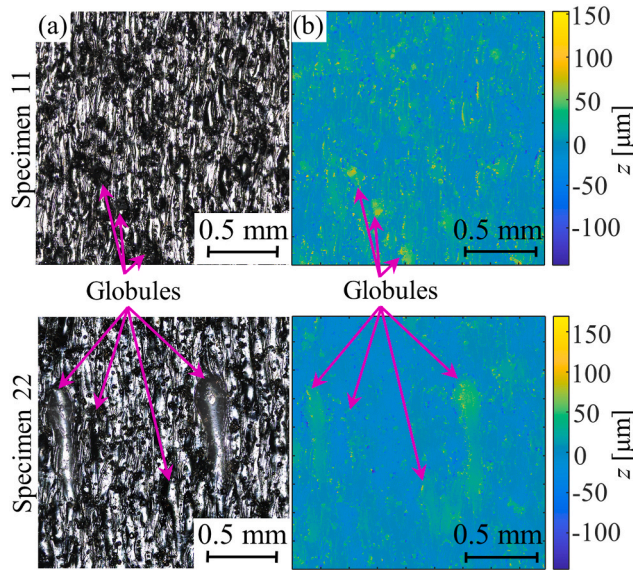


Fig. 4. (a) Optical microscopy images and (b) corresponding surface topography maps $z = f(x,y)$ for as-built surface S1 of specimen 11 ($\alpha = 90^\circ$, $t = 30 \mu\text{m}$, $E_p = 47.5 \text{ J/mm}^3$) and specimen 22 ($\alpha = 90^\circ$, $t = 60 \mu\text{m}$, $E_p = 50.0 \text{ J/mm}^3$), identifying an increasing number and size of globules with increasing layer thickness.

scan speed to maintain constant energy density E_p during the L-PBF process. This can overheat the melt pool, which increases the temperature gradient between the melt pool and the previously melted tracks, and the hot molten metal flows towards the cold already solidified material (“Marangoni effect”), thus creating globules [54]. These results are in agreement with those of Lou et al. who determined that surfaces with globules show 3.5% and 9.3% higher average roughness S_a and root mean square deviation S_q , respectively, compared to surfaces without globules [38]. Fig. 4 (a) depicts optical microscopy images and Fig. 4 (b) shows the corresponding surface topography maps $z = f(x,y)$ for as-built surface S1 of specimen 11 ($\alpha = 90^\circ$, $t = 30 \mu\text{m}$, $E_p = 47.5 \text{ J/mm}^3$) and specimen 22 ($\alpha = 90^\circ$, $t = 60 \mu\text{m}$, $E_p = 50.0 \text{ J/mm}^3$).

From Fig. 4, we observe four large, smooth globules, the largest approximately $200 \mu\text{m}$ by $750 \mu\text{m}$, on S1 of specimen 22 ($t = 60 \mu\text{m}$), whereas we observe three small globules, approximately $100 \mu\text{m}$ by $100 \mu\text{m}$, on S1 of specimen 11 ($t = 30 \mu\text{m}$). Fig. 4 (b) shows that the globules protrude approximately $100 \mu\text{m}$ – $150 \mu\text{m}$ above the mean surface topography plane. These results are typical for all specimens in this work.

3.4. Surface topography parameters as a function of build orientation

Fig. 5 schematically illustrates the specimens on the build plate with

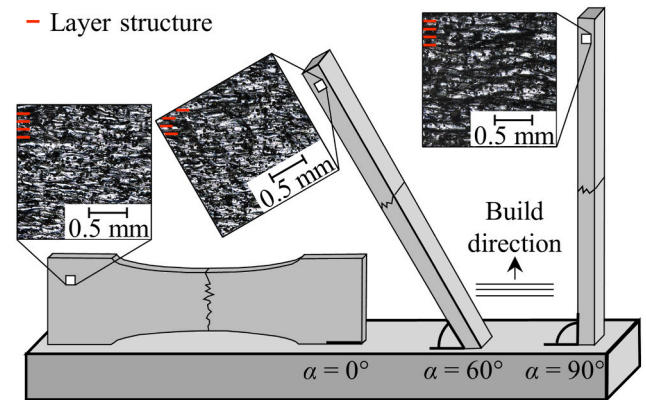


Fig. 5. Schematic of fatigue specimens with build orientations $\alpha = 0^\circ$, 60° , and 90° . Inset optical microscopy images show the layer-upon-layer structure of each specimen.

build orientations $\alpha = 0^\circ$, 60° , and 90° , and with inset optical microscopy images that show their layer-upon-layer structure in the build direction.

Table 8 shows the average and standard deviation of the 9 PP deterministic surface topography parameters (η , R_s , and σ_s) for as-built surfaces (S1–S4) of the specimens. We do not include S5 because the surface topography of the top as-built surface remains almost independent of the build orientation, as we showed in Table 4. Note also that specimens with $\alpha = 0^\circ$ do not have as-built surfaces S1 and S2.

From Table 8, we observe that the average values of summit density η and mean summit radius R_s decrease and the standard deviation of summit heights σ_s increases when comparing build orientations $\alpha = 60^\circ$ to $\alpha = 90^\circ$ for up-facing surfaces (S1). In contrast, the average values of the summit density η and mean summit radius R_s increase and the standard deviation of summit heights σ_s decreases for down-facing surfaces (S2), and mean summit radius R_s increase for side (S3 and S4) as-built surfaces when comparing build orientations $\alpha = 60^\circ$ to $\alpha = 90^\circ$. The average values of summit density η and the standard deviation of summit heights σ_s do not change when comparing build orientations $\alpha = 60^\circ$ to $\alpha = 90^\circ$ for side (S3 and S4) as-built surfaces.

Specimens with build orientations $\alpha = 0^\circ$ and $\alpha = 90^\circ$ are fundamentally different than those with $\alpha > 0^\circ$ and $\alpha < 90^\circ$; e.g. in this work we use $\alpha = 60^\circ$. When $\alpha = 0^\circ$ and $\alpha = 90^\circ$, a new layer builds entirely upon a previously solidified layer, whereas when $0^\circ < \alpha < 90^\circ$ a new layer partially builds upon unsupported metal powder particles. When $0^\circ < \alpha < 90^\circ$, we observe the staircase-effect, which is particularly visible in the up-facing as-built surfaces. Additionally, unmelted (partially melted) metal powder particles can more easily adhere to the up- and down-facing surfaces because the heat flux is not entirely directed towards previously solidified material, but unsupported metal powder particles instead, as previously documented in Refs. [16,25].

Table 8

Average and standard deviation of 9 PP deterministic surface topography parameters: η , R_s , and σ_s for different build orientation $\alpha = 0^\circ$, 60° , and 90° , for as-built surfaces (S1–S4). Specimens with $\alpha = 0^\circ$ do not have as-built surfaces S1 and S2.

| Average/ Standard deviation | S1 | | | S2 | | | S3 | | | S4 | | |
|-----------------------------------|--------------------|---------------------|---------------------|--------------------|---------------------|---------------------|--------------------|---------------------|---------------------|--------------------|---------------------|---------------------|
| | $\alpha = 0^\circ$ | $\alpha = 60^\circ$ | $\alpha = 90^\circ$ | $\alpha = 0^\circ$ | $\alpha = 60^\circ$ | $\alpha = 90^\circ$ | $\alpha = 0^\circ$ | $\alpha = 60^\circ$ | $\alpha = 90^\circ$ | $\alpha = 0^\circ$ | $\alpha = 60^\circ$ | $\alpha = 90^\circ$ |
| η (9 PP) | – | 0.148/ 0.012 | 0.135/ 0.018 | – | 0.129/ 0.012 | 0.149/ 0.023 | 0.125/ 0.020 | 0.147/ 0.019 | 0.147/ 0.020 | 0.130/ 0.016 | 0.142/ 0.014 | 0.148/ 0.021 |
| R_s (9 PP) | – | 0.105/ 0.008 | 0.093/ 0.012 | – | 0.081/ 0.012 | 0.107/ 0.014 | 0.088/ 0.016 | 0.092/ 0.015 | 0.097/ 0.011 | 0.093/ 0.012 | 0.092/ 0.013 | 0.099/ 0.012 |
| σ_s (9 PP) | – | 6.469/ 0.905 | 7.963/ 2.154 | – | 9.238/ 1.750 | 6.438/ 1.896 | 9.883/ 2.704 | 7.720/ 2.102 | 7.341/ 1.786 | 8.993/ 1.813 | 7.756/ 1.842 | 7.066/ 1.634 |

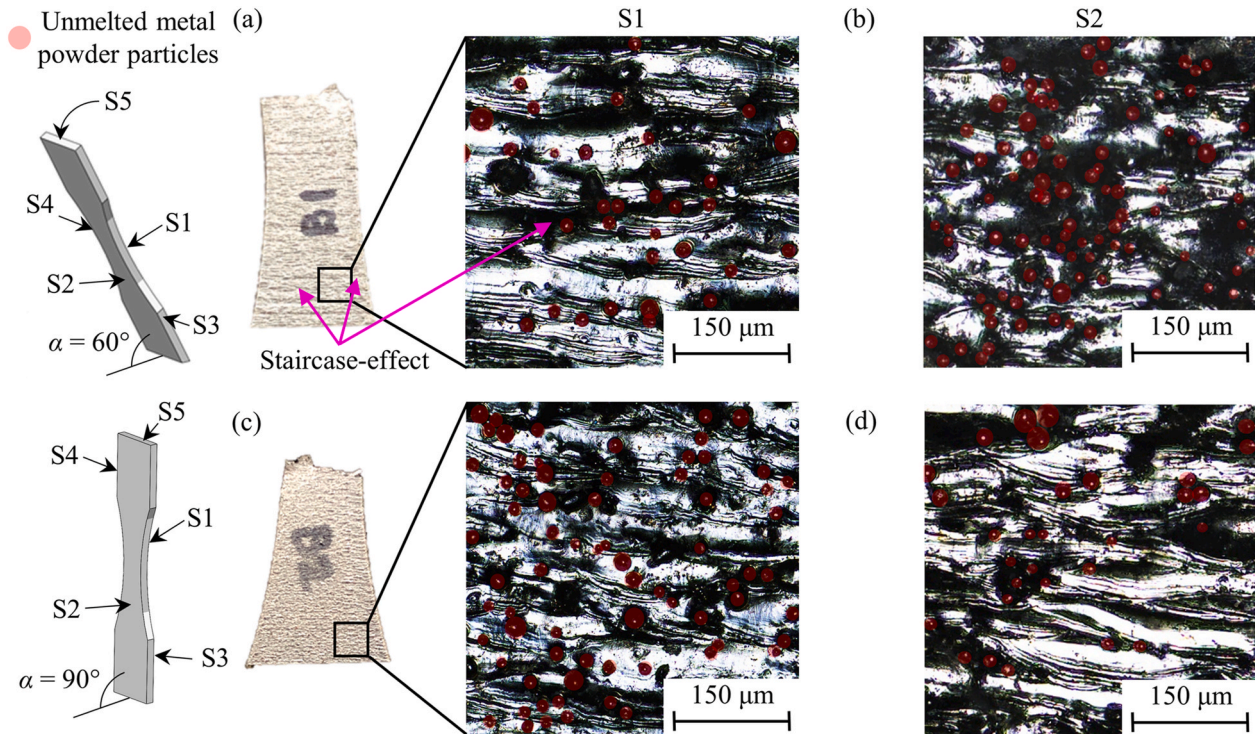


Fig. 6. (a) Photograph of specimen 14 ($\alpha = 60^\circ$, $t = 60 \mu\text{m}$, $E_p = 50.0 \text{ J/mm}^3$) with optical microscopy image of S1, (b) optical microscopy image of S2 of specimen 1 ($\alpha = 60^\circ$, $t = 30 \mu\text{m}$, $E_p = 62.2 \text{ J/mm}^3$) (c) photograph of specimen 23 ($\alpha = 90^\circ$, $t = 60 \mu\text{m}$, $E_p = 50.0 \text{ J/mm}^3$) with optical microscopy image of S1 (d) optical microscopy images of S2 of specimen 11 ($\alpha = 90^\circ$, $t = 30 \mu\text{m}$, $E_p = 47.5 \text{ J/mm}^3$), illustrating a higher and lower density of unmelted metal powder particles (highlighted in red) on as-built surface S1 and S2 for specimens with $\alpha = 60^\circ$ and $\alpha = 90^\circ$, respectively. (For interpretation of the references to colour in this figure legend, the reader is referred to the Web version of this article.)

Fig. 6 illustrates the effect of the build orientation ($\alpha = 60^\circ$ and $\alpha = 90^\circ$) on the number of unmelted metal powder particles that adhere to the different as-built surfaces. Fig. 6 (a) and (c) show photographs of specimens 14 ($\alpha = 60^\circ$, $t = 60 \mu\text{m}$, $E_p = 50.0 \text{ J/mm}^3$) and 23 ($\alpha = 90^\circ$, $t = 60 \mu\text{m}$, $E_p = 50.0 \text{ J/mm}^3$), respectively, with optical microscopy images of an up-facing as-built surface (S1). Fig. 6 (b) and (d) show optical microscopy images of down-facing as-built surface (S2) of specimen 1 ($\alpha = 60^\circ$, $t = 30 \mu\text{m}$, $E_p = 62.2 \text{ J/mm}^3$) and specimen 11 ($\alpha = 90^\circ$, $t = 30 \mu\text{m}$, $E_p = 47.5 \text{ J/mm}^3$), respectively. We also schematically illustrate the orientation of each specimen ($\alpha = 60^\circ$ and $\alpha = 90^\circ$) and its up-facing (S1) and down-facing (S2) as-built surfaces. From Fig. 6 (a) and (c) we observe fewer unmelted metal powder particles on S1 of specimen 14 with $\alpha = 60^\circ$ (approximately 156.7 unmelted metal powder particles/ mm^2) than on S1 of specimen 23 with $\alpha = 90^\circ$ (approximately 350.0 unmelted metal powder particles/ mm^2), because S1 of specimen 14 is entirely built on top of previously solidified material. These results explain the experimental data of Table 8, which indicate that the surface roughness of as-built surfaces S1 with $\alpha = 90^\circ$ is greater than with $\alpha = 60^\circ$. Conversely, from Fig. 6 (b) and (d) we observe more unmelted

metal powder particles on S2 of specimen 1 with $\alpha = 60^\circ$ (approximately 433.6 unmelted metal powder particles/ mm^2) than on S2 of specimen 11 with $\alpha = 90^\circ$ surface of specimen 11 (approximately 141.1 unmelted metal powder particles/ mm^2). Heat flux into previously solidified material layers is greater for the specimens built parallel to the build direction than the specimens built at $\alpha = 60^\circ$ [16,25] and, thus, fewer unmelted metal powder particles adhere to S2 of specimens with $\alpha = 90^\circ$ than with $\alpha = 60^\circ$. These results also explain that the surface roughness of as-built surfaces S2 with $\alpha = 60^\circ$ is greater than with $\alpha = 90^\circ$ (Table 8). Note also that the unmelted metal powder particle density on S1 and S2 of specimens with $\alpha = 90^\circ$ is almost identical, because physically these surfaces are similar, i.e., parallel to the build direction and orthogonal to the top surface, even though the labeling system in this work refers to them as up- and down-facing, respectively.

The surface topography of the up-facing as-built surfaces (S1) is in agreement with the results obtained by Strano et al., who showed that the staircase-effect geometry of the layer-upon-layer fabrication drives the average roughness R_a of the up-facing as-built surfaces [24]. Similarly, the surface topography of the down-facing as-built surfaces (S2) is

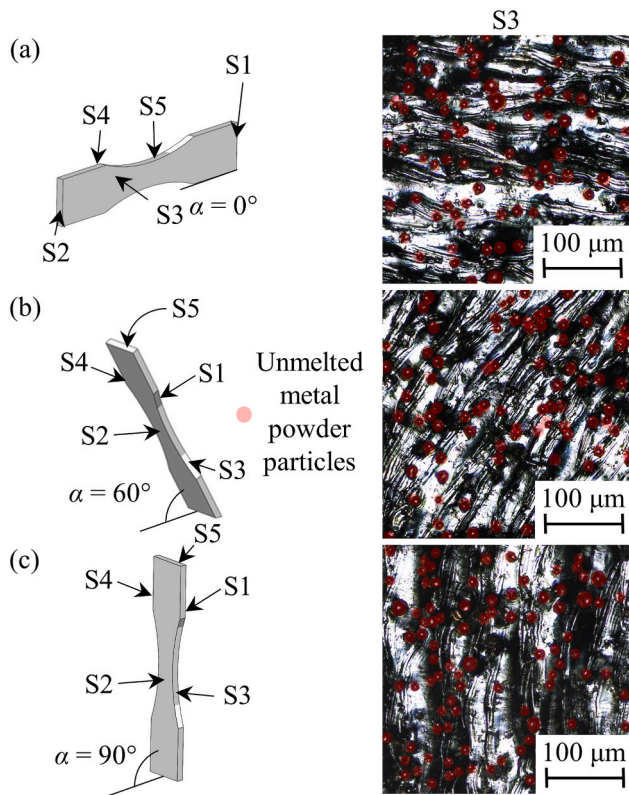


Fig. 7. Optical microscopy images of as-built surfaces at the gas flow inlet (S3) with different build orientations, showing (a) specimen 15 ($\alpha = 0^\circ$, $t = 60 \mu\text{m}$, $E_p = 32.4 \text{ J/mm}^3$), (b) specimen 18 ($\alpha = 60^\circ$, $t = 60 \mu\text{m}$, $E_p = 32.0 \text{ J/mm}^3$), and (c) specimen 24 ($\alpha = 90^\circ$, $t = 60 \mu\text{m}$, $E_p = 33.3 \text{ J/mm}^3$).

in agreement with the results presented by Fox et al., who showed that adhesion of unmelted metal powder particles (highlighted in red) drives the surface topography parameters of the down-facing as-built surfaces [26].

Fig. 7 (a), (b), and (c) show optical microscopy images of the as-built surface (S3) at the gas flow inlet of specimens 15 ($\alpha = 0^\circ$, $t = 60 \mu\text{m}$, $E_p = 32.4 \text{ J/mm}^3$), 18 ($\alpha = 60^\circ$, $t = 60 \mu\text{m}$, $E_p = 32.0 \text{ J/mm}^3$), and 24 ($\alpha = 90^\circ$, $t = 60 \mu\text{m}$, $E_p = 33.3 \text{ J/mm}^3$), respectively, illustrating the density of unmelted metal powder particles (highlighted in red) on S3 as a function of the different build orientations used in this work. We also schematically illustrate the orientation of each specimen ($\alpha = 0^\circ$, $\alpha = 60^\circ$, and $\alpha = 90^\circ$) and its different as-built surfaces S1–S5.

We qualitatively observe from Fig. 7 (a) that unmelted metal powder particles appear uniformly distributed on the S3 as-built surface of specimens with $\alpha = 0^\circ$. In contrast, from Fig. 7 (b) and (c) we observe that the unmelted metal powder particles agglomerate around the layer-upon-layer interfaces on the S3 as-built surface of specimens with $\alpha = 60^\circ$ and $\alpha = 90^\circ$. The density of unmelted metal powder particles is independent of the build orientation $\alpha = 0^\circ$ (624.9 unmelted metal powder particles/mm²), 60° (653.3 unmelted metal powder particles/mm²), and 90° (681.7 unmelted metal powder particles/mm²). The unmelted metal powder particles carried by the gas flow settle at the interfaces of the layer-upon-layer structure for specimens with $\alpha = 60^\circ$ and $\alpha = 90^\circ$ specimens and, thus, the surface roughness of specimens with build orientations $\alpha = 60^\circ$ and $\alpha = 90^\circ$ is lower than that of specimens with build orientation $\alpha = 0^\circ$, where the unmelted metal powder particles do not preferentially settle at the interfaces of the layer-upon-layer structure. We observe similar results for the as-built surface at the gas flow outlet (S4). These observations explain the experimental data of Tables 8 and i.e., the surface roughness of as-built

surfaces S3 and S4 is higher for specimens with $\alpha = 0^\circ$ than for specimens with $\alpha = 60^\circ$ and 90° .

4. Conclusions

We have determined the relationship between the surface topography parameters of as-built Inconel 718 surfaces and their corresponding L-PBF process parameters using multivariate regression analysis with traditional R - and S -parameters, statistical, and deterministic parameters, and even combinations of surface topography parameters, to determine which parameters most closely relate to the L-PBF process parameters. We conclude that:

- 1) The deterministic surface topography parameters (η , R_s , and σ_s), derived from the 9 PP scheme result in the best-fit regression equations with the highest adjusted- R^2 and, thus, show the closest relationship to the L-PBF process parameters, when considering one dataset of all as-built surfaces (S1–S5), and when considering each as-built surface separately. However, the adjusted- R^2 values of the best-fit regression equations are substantially higher when considering the different as-built surfaces separately as opposed to aggregating them into one dataset. This is because the surface topography of the different as-built surfaces is distinctly different due to their location and orientation on the build plate with respect to the gas flow and recoater directions. In contrast to the R -, S -, and statistical parameters, the deterministic approach considers the actual peaks of the surface topography rather than relying on a discrete number of traces of the surface and, thus, includes the most detailed information of the surface topography. This conclusion is different from existing knowledge of the surface topography of as-built L-PBF surfaces, which rely on traditional R - and S -parameters.
- 2) The surface roughness expressed using deterministic surface topography parameters decreases with increasing layer thickness, but the number of peaks increases with increasing layer thickness because of increased globule formation. Globules result from increasing bulk laser power or decreasing scan speed to maintain the laser energy density within the recommended range when increasing the layer thickness.
- 3) The surface roughness expressed using deterministic surface topography parameters of the up-facing (S1) as-built surfaces increases and of the down-facing (S2) as-built surfaces decreases, for specimens with a build orientation different than $\alpha = 0^\circ$ and $\alpha = 90^\circ$ (i.e., $\alpha = 60^\circ$ in this work). The presence of unmelted metal powder particles dominates the surface topography of the down-facing as-built surfaces, whereas the staircase-effect dominates the surface topography of the up-facing as-built surfaces.

Declaration of competing interest

The authors declare that they have no known competing financial interests or personal relationships that could have appeared to influence the work reported in this paper.

Acknowledgments

We gratefully acknowledge support from the Department of Defense, Office of Local Defense Community Cooperation, under award no. ST1605-19-03. Furthermore, we thank Prof. Wenda Tan for fruitful discussions about this research.

Appendix A. Supplementary data

Supplementary data to this article can be found online at <https://doi.org/10.1016/j.precisioneng.2021.12.003>.

References

- [1] Ngo TD, Kashani A, Imbalzano G, Nguyen KTQ, Hui D. Additive manufacturing (3D printing): a review of materials, methods, applications and challenges. *Compos Part B* 2018;143:172–96. <https://doi.org/10.1016/j.compositesb.2018.02.012>.
- [2] Additive manufacturing — process characteristics and performance — practice for metal powder bed fusion process to meet critical applications, ISO/ASTM 52904, 2019 n.d.
- [3] Gibson I, Rosen D, Stucker B. Additive manufacturing technologies: 3D printing, rapid prototyping, and direct digital manufacturing. second ed. New York, NY: Springer US; 2015. <https://doi.org/10.2495/SDP-V9-N5-658-668>.
- [4] Kruth JP, Leu Mc, Nakagawa T. Progress in additive manufacturing and rapid prototyping. *Ann. CIRP* 1998;47:12–24. <https://doi.org/10.1007/s40962-019-00340-1>.
- [5] Nath C, Brooks Z, Kurfess TR. Machinability study and process optimization in face milling of some super alloys with indexable copy face mill inserts. *J Manuf Process* 2015;20:88–97. <https://doi.org/10.1016/j.jmapro.2015.09.006>.
- [6] Tian Z, Zhang C, Wang D, Liu W, Fang X, Wellman D, et al. A review on laser powder bed fusion of inconel 625. *Appl Sci* 2019;10:81.
- [7] Singh S, Ramakrishna S. Biomedical applications of additive manufacturing: present and future. *Curr Opin Biomed Eng* 2017;2:105–15. <https://doi.org/10.1016/j.cobme.2017.05.006>.
- [8] Rochus P, Plessier JY, Van Elsen M, Kruth JP, Carrus R, Dormal T. New applications of rapid prototyping and rapid manufacturing (RP/RM) technologies for space instrumentation. *Acta Astronaut* 2007;61:352–9. <https://doi.org/10.1016/j.actaastro.2007.01.004>.
- [9] Martin JH, Yahata BD, Hundley JM, Mayer JA, Schaedler TA, Pollock TM. 3D printing of high-strength aluminium alloys. *Nature* 2017;549:365–9. <https://doi.org/10.1038/nature23894>.
- [10] Frazier WE. Metal additive manufacturing: a review. *J Mater Eng Perform* 2014;23:1917–28. <https://doi.org/10.1007/s11665-014-0958-z>.
- [11] Kumbhar NN, Mulay AV. Post processing methods used to improve surface finish of products which are manufactured by additive manufacturing technologies: a review. *J Inst Eng Ser C* 2018;99:481–7. <https://doi.org/10.1007/s40032-016-0340-z>.
- [12] Jiang R, Mostafaei A, Pauza J, Kantzos C, Rollett AD. Varied heat treatments and properties of laser powder bed printed Inconel 718. *Mater Sci Eng, A* 2019;755:170–80. <https://doi.org/10.1016/j.msea.2019.03.103>.
- [13] Carter LN, Martin C, Withers PJ, Attallah MM. The influence of the laser scan strategy on grain structure and cracking behaviour in SLM powder-bed fabricated nickel superalloy. *J Alloys Compd* 2014;615:338–47. <https://doi.org/10.1016/j.jallcom.2014.06.172>.
- [14] Newell DJ, O'Hara RP, Cobb GR, Palazotto AN, Kirka MM, Burggraf LW, et al. Mitigation of scan strategy effects and material anisotropy through supersolvus annealing in LPBF IN718. *Mater Sci Eng, A* 2019;764:138230. <https://doi.org/10.1016/j.msea.2019.138230>.
- [15] Lee SC, Chang SH, Tang TP, Ho HH, Chen JK. Improvement in the microstructure and tensile properties of inconel 718 superalloy by HIP treatment. *Mater Trans* 2006;47:2877–81. <https://doi.org/10.2320/matertrans.47.2877>.
- [16] Pyka G, Kerckhofs G, Papanoniu I, Speirs M, Schrooten J, Wevers M. Surface roughness and morphology customization of additive manufactured open porous Ti6Al4V structures. *Materials (Basel)* 2013;6:4737–57. <https://doi.org/10.3390/ma6104737>.
- [17] Mohammadian N, Turenne S, Brailovski V. Surface finish control of additively-manufactured Inconel 625 components using combined chemical-abrasive flow polishing. *J Mater Process Technol* 2018;252:728–38. <https://doi.org/10.1016/j.jmatprotec.2017.10.020>.
- [18] Calignano F, Manfredi D, Ambrosio EP, Iuliano L, Fino P. Influence of process parameters on surface roughness of aluminum parts produced by DMLS. *Int J Adv Manuf Technol* 2013;67:2743–51. <https://doi.org/10.1007/s00170-012-4688-9>.
- [19] Lesyk DA, Martinez S, Mordiyuk BN, Dzhemelinskiy VV, Lamikiz Prokopenko GI. Post-processing of the Inconel 718 alloy parts fabricated by selective laser melting: effects of mechanical surface treatments on surface topography, porosity, hardness and residual stress. *Surf Coating Technol* 2020;381:125136. <https://doi.org/10.1016/j.surfcoat.2019.125136>.
- [20] Liu B, Fang G, Lei L. An analytical model for rapid predicting molten pool geometry of selective laser melting (SLM). *Appl Math Model* 2021;92:505–24. <https://doi.org/10.1016/j.apm.2020.11.027>.
- [21] Keshavarzkermani A, Marzbanrad E, Esmaeilzadeh R, Mahmoodkhani Y, Ali U, Enrique PD, et al. An investigation into the effect of process parameters on melt pool geometry, cell spacing, and grain refinement during laser powder bed fusion. *Opt Laser Technol* 2019;116:83–91. <https://doi.org/10.1016/j.optlastec.2019.03.012>.
- [22] Triantaphyllou A, Giusca CL, Macaulay GD, Roerig F, Hoebel M, Leach RK, et al. Surface texture measurement for additive manufacturing. *Surf Topogr Metrol Prop* 2015;3. <https://doi.org/10.1088/2051-672X/3/2/024002>.
- [23] Eidt W, Tatman EP, McCarther J, Kastner J, Gunther S, Gockel J. Surface roughness characterization in laser powder bed fusion additive manufacturing. *Solid Free. Fabr. In: Proc. 30th annu. Int. Solid free. Fabr. Symp. - an addit. Manuf. Conf. SFF. vol. 2019; 2019. p. 2165–76. 2019*
- [24] Strano G, Hao L, Everson RM, Evans KE. Surface roughness analysis, modelling and prediction in selective laser melting. *J Mater Process Technol* 2013;213:589–97. <https://doi.org/10.1016/j.jmatprotec.2012.11.011>.
- [25] Charles A, Elkaseer A, Thijs L, Hagemeyer V, Scholz S. Effect of process parameters on the generated surface roughness of down-facing surfaces in selective laser melting. *Appl Sci* 2019;9:1256. <https://doi.org/10.3390/app9061256>.
- [26] Fox JC, Moylan SP, Lane BM. Effect of process parameters on the surface roughness of overhanging structures in laser powder bed fusion additive manufacturing. Elsevier B.V. *Procedia CIRP* 2016;vol. 45:131–4. <https://doi.org/10.1016/j.procir.2016.02.347>.
- [27] Safdar A, He HZ, Wei LY, Snis A, Chavez De Paz LE. Effect of process parameters settings and thickness on surface roughness of EBM produced Ti-6Al-4V. *Rapid Prototyp J* 2012;18:401–8. <https://doi.org/10.1108/13552541211250391>.
- [28] Galati M, Rizza G, Defanti S, Denti L. Surface roughness prediction model for Electron Beam Melting (EBM) processing Ti6Al4V. *Precis Eng* 2021;69:19–28. <https://doi.org/10.1016/j.precisioneng.2021.01.002>.
- [29] Whip B, Sheridan L, Gockel J. The effect of primary processing parameters on surface roughness in laser powder bed additive manufacturing. *Int J Adv Manuf Technol* 2019;103:4411–22. <https://doi.org/10.1007/s00170-019-03716-z>.
- [30] Khorasani AM, Gibson I, Ghasemi AH, Ghaderi A. Modelling of laser powder bed fusion process and analysing the effective parameters on surface characteristics of Ti-6Al-4V. *Int J Mech Sci* 2020;168:105299. <https://doi.org/10.1016/j.ijmeccsi.2019.105299>.
- [31] Özel T, Altay A, Kaftanoğlu B, Leach R, Senin N, Donmez A. Focus variation measurement and prediction of surface texture parameters using machine learning in laser powder bed fusion. *J Manuf Sci Eng* 2020;142. <https://doi.org/10.1115/1.4054515>.
- [32] Mate CM. Tribology on the small scale: a bottom up approach to friction, lubrication, and wear. New York, NY: Oxford University Press; 2008.
- [33] ASTM F1877. Standard practice for characterization of particles. Standard; 2016 [n.d].
- [34] ASTM E466-07. Standard practice for conducting force controlled constant amplitude axial fatigue tests of metallic materials, n.d. Standard; 2007.
- [35] Watring DS, Carter KC, Crouse D, Raeymaekers B, Spear AD. Mechanisms driving high-cycle fatigue life of as-built Inconel 718 processed by laser powder bed fusion. *Mater Sci Eng, A* 2019;761:137993. <https://doi.org/10.1016/j.msea.2019.06.003>.
- [36] Watring DS, Benzing JT, Hrabe N, Spear AD. Effects of laser-energy density and build orientation on the structure–property relationships in as-built Inconel 718 manufactured by laser powder bed fusion. *Addit Manuf* 2020;36:101425. <https://doi.org/10.1016/j.addma.2020.101425>.
- [37] Wirth F, Frauchiger A, Gutknecht K, Cloots M. Influence of the inert gas flow on the laser powder bed fusion (LPBF) process. *Industrial. Springer International Publishing*; 2021. <https://doi.org/10.1007/978-3-030-54334-1>.
- [38] Lou S, Jiang X, Sun W, Zeng W, Pagani L, Scott PJ. Characterisation methods for powder bed fusion processed surface topography. *Precis Eng* 2019;57:1–15. <https://doi.org/10.1016/j.precisioneng.2018.09.007>.
- [39] Townsend A, Senin N, Blunt L, Leach RK, Taylor JS. Surface texture metrology for metal additive manufacturing: a review. *Precis Eng* 2016;46:34–47. <https://doi.org/10.1016/j.precisioneng.2016.06.001>.
- [40] Leach RK, Bourell D, Carmignato S, Donmez A, Senin N, Dewulf W. Geometrical metrology for metal additive manufacturing. *CIRP Ann* 2019;68:677–700. <https://doi.org/10.1016/j.cirp.2019.05.004>.
- [41] ISO 25178-2 2012 “Geometrical product specification (GPS) - surface texture: areal - Part 2: terms, definitions and surface texture parameters” n.d.
- [42] ISO 4287. Geometrical product specification (GPS): surface texture: profile method: terms, definitions and surface texture parameters.n.d. British Standards Institute; 2000.
- [43] Pawar G, Pawlus P, Etsion I, Raeymaekers B. The effect of determining topography parameters on analyzing elastic contact between isotropic rough surfaces. *J Tribol* 2013;135:1–10. <https://doi.org/10.1115/1.4007760>.
- [44] McCool JI. Relating profile instrument measurements to the functional performance of rough surfaces. *ASME J Tribol* 1987;109:264–70.
- [45] Kalin M, Pogačnik A, Etsion I, Raeymaekers B. Comparing surface topography parameters of rough surfaces obtained with spectral moments and deterministic methods. *Tribol Int* 2016;93:137–41. <https://doi.org/10.1016/j.triboint.2015.09.013>.
- [46] Sen A, Srivastava M. Regression analysis: theory, methods, and applications. New York: Springer-Verlag; 1990.
- [47] Hair J, Black B, Babin B, Anderson R. Multivariate data analysis. seventh ed. Upper Saddle River, NJ: Pearson Education; 2010.
- [48] Montgomery D. Design and analysis of experiments. Fifth: John Wiley & Sons, Inc.; 1997.
- [49] Willmott C, Ackleson G, Davis E, Feddema J, Klink M, Legates DR, et al. Statistics for the evaluation and comparison of models. *J Geophys Res* 1985;90:8995–9005. [https://doi.org/10.1016/0198-0254\(86\)91285-9](https://doi.org/10.1016/0198-0254(86)91285-9).
- [50] Botchkarev A. A new typology design of performance metrics to measure errors in machine learning regression algorithms. *Interdiscipl J Inf Knowl Manag* 2019;14:45–76. <https://doi.org/10.28945/4184>.
- [51] Yadroitsev I, Gusarov A, Yadroitsava I, Smurov I. Single track formation in selective laser melting of metal powders. *J Mater Process Technol* 2010;210:1624–31. <https://doi.org/10.1016/j.jmatprotec.2010.05.010>.

- [52] Chen Z, Wu X, Tomus D, Davies CHJ. Surface roughness of selective laser melted Ti-6Al-4V alloy components. *Addit Manuf* 2018;21:91–103. <https://doi.org/10.1016/j.addma.2018.02.009>.
- [53] Li X, Zhao C, Sun T, Tan W. Revealing transient powder-gas interaction in laser powder bed fusion process through multi-physics modeling and high-speed synchrotron x-ray imaging. *Addit Manuf* 2020;35:101362. <https://doi.org/10.1016/j.addma.2020.101362>.
- [54] Simonelli M, Tuck C, Aboulkhair NT, Maskery I, Ashcroft I, Wildman RD, et al. A study on the laser spatter and the oxidation reactions during selective laser melting of 316L stainless steel, Al-Si10-Mg, and Ti-6Al-4V. *Metall Mater Trans A* 2015;46:3842–51. <https://doi.org/10.1007/s11661-015-2882-8>.